Acta Pharmaceutica Sinica B 2022;12(3):1487−1499

Chinese Pharmaceutical Association
Institute of Materia Medica, Chinese Academy of Medical Sciences

Acta Pharmaceutica Sinica B

www.elsevier.com/locate/apsb
www.sciencedirect.com

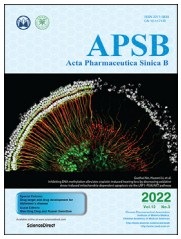

ORIGINAL ARTICLE

Artificial tumor microenvironment regulated by first hemorrhage for enhanced tumor targeting and then occlusion for synergistic bioactivation of hypoxia-sensitive platesomes

Wenhui Tao[a], Dongyang Zhao[a], Guanting Li[a], Lingxiao Li[a], Songhao Li[a], Hao Ye[a], Chutong Tian[a], Yutong Lu[a], Shuying Li[b], Yinghua Sun[c], Zhonggui He[a], Jin Sun[a,*]

[a]*Department of Pharmaceutics, Wuya College of Innovation, Shenyang Pharmaceutical University, Shenyang 110016, China*
[b]*Department of Pharmaceutical and Engineering, College of Pharmaceutical and Engineering, Shenyang Pharmaceutical University, Shenyang 110016, China*
[c]*Department of Pharmaceutics, College of Pharmacy, Shenyang Pharmaceutical University, Shenyang 110016, China*

Received 18 April 2021; received in revised form 20 June 2021; accepted 3 July 2021

KEY WORDS

Tumor microenvironment;
Vascular disrupting agents;
Biomimetic platesomes;
Photosensitizers;
Hypoxia-activated prodrugs;
Nanomedicine delivery;
Combination therapy;
Antitumor and antimetastasis

Abstract The unique characteristics of the tumor microenvironment (TME) could be exploited to develop antitumor nanomedicine strategies. However, in many cases, the actual therapeutic effect is far from reaching our expectations due to the notable tumor heterogeneity. Given the amplified characteristics of TME regulated by vascular disrupting agents (VDAs), nanomedicines may achieve unexpected improved efficacy. Herein, we fabricate platelet membrane-fusogenic liposomes (PML/DP&PPa), namely "platesomes", which actively load the hypoxia-activated pro-prodrug DMG-PR104A (DP) and physically encapsulate the photosensitizer pyropheophorbide a (PPa). Considering the different stages of tumor vascular collapse and shutdown induced by a VDA combretastatin-A4 phosphate (CA4P), PML/DP&PPa is injected 3 h after intraperitoneal administration of CA4P. First, CA4P-mediated tumor hemorrhage amplifies the enhanced permeation and retention (EPR) effect, and the platesome-biological targeting further promotes the tumor accumulation of PML/DP&PPa. Besides, CA4P-induced vascular occlusion inhibits oxygen supply, followed by photodynamic therapy-caused acute tumor hypoxia. This prolonged extreme hypoxia contributes to the complete activation of DP and then high inhibitory effect on tumor growth and

*Corresponding author. Tel./fax: +86 24 23986321.
E-mail address: sunjin@syphu.edu.cn (Jin Sun).

Peer review under responsibility of Chinese Pharmaceutical Association and Institute of Materia Medica, Chinese Academy of Medical Sciences.

https://doi.org/10.1016/j.apsb.2021.08.010

metastasis. Thus, such a combining strategy of artificially-regulated TME and bio-inspired platesomes pronouncedly improves tumor drug delivery and boosts tumor hypoxia-selective activation, and provides a preferable solution to high-efficiency cancer therapy.

1. Introduction

Nanomedicines could accumulate preferentially in tumors by the enhanced permeability and retention (EPR) effect due to defective tumor vasculature and impaired lymphatic drainage[1,2]. However, given significant tumor heterogeneity, the nanomedicines' EPR effect is quite inconsistent between preclinical animal models and patients[3,4]. Hence, the researchers focus upon optimizing the tumor targeting of nanomedicines *via* modifying targeting ligands or tumor penetrating peptides, especially cell membrane modification[5–7]. Among these biomimetic nanoplatforms, nanoplatelets are presently in the spotlight owing to their high biocompatibility, less toxicity, and indispensable role in the process of coagulation[8,9]. In addition, we have found that platelet-inspired nanosystems could actively target tumor tissues mainly *via* specific interaction between the P-selectin of platelets and the over-expressed CD44 receptor on cancerous cell[10,11]. If the platelet membrane is incorporated into the phospholipid bilayer membrane of liposomes, as a more biomimetic cell-membrane-mimicking nano-cargoes, the fabricated "platesomes" might both inherit the biological properties of platelet and high drug loading capacity and long-circulating function of liposomes. Nevertheless, the off-target effect caused by complex tumor heterogeneity between different types of tumors greatly compromises the tumor targeting efficiency[1]. Therefore, this underscores the importance of artificially remodeling the tumor microenvironment (TME) to reduce tumor heterogeneity and increase tumor targeting[12–14].

As is known, combretastatin-A4 phosphate (CA4P), a kind of vascular disrupting agents (VDAs), could rapidly and selectively destroy tumor blood vessels[15–17]. The CA4P-induced hemorrhage is an early result of structural collapse of the tumor vasculatures, and recent studies have suggested that the EPR effect could be magnified by this unique tumor-hemorrhagic strategy[18,19]. In addition, the direct exposure of abnormal basement membrane after treatment with VDAs could provide opportunities for the interaction of platelets and collagen within coagulation[20]. Thus, the cooperation of bio-inspired nanoplatelets and VDAs is more likely to exhibit unique superiority to achieve efficient tumoral drug delivery.

Hypoxia is a fundamental feature of TME, which provides the fuel for resistance to chemotherapy and radiotherapy[21,22]. Hypoxia-activated prodrugs (HAPs) have emerged to utilize the hypoxic condition of TME[23]. In order to avoid the off-target activation in the normal tissues, the phosphate ester dinitrobenzamide mustard PR104A, as a HAP, has attracted widespread attention with a more stringent activation oxygen partial pressures range of 1–5 mm Hg[24,25]. However, due to the heterogeneity of hypoxia between the outer and inner tumors, the activation of HAPs is often insufficient. Therefore, various strategies are adopted to aggravate tumor hypoxia, including photodynamic therapy (PDT)[26], glucose oxidase-based starvation therapy[27], and vasculature disruption therapy[28]. In our previous study, self-assembled prodrug-nanoparticles were developed by a thioketal-bridged PR104A-pyropheophorbide a (PPa) prodrug for synergistic photodynamic and hypoxia-activated therapy[26]. However, we found that although PDT could quickly consume tumor oxygen after laser irradiation and cause acute hypoxia, the hypoxia tended to return to the normal level over time gradually. Luckily, at a later stage of administration VDAs, a cascade of events like coagulation, narrowing blood vessel and increased blood viscosity caused the final vascular occlusion with induced hypoxia in tumor[28]. If PDT is combined with VDAs, the persistent and severe tumor hypoxia could exist to a great extent. In addition, the lower degree of hypoxia, the more complete bioactivation of HAPs.

Herein, we prepared *N*,*N*-dimethylglycine (DMG)-PR104A conjugate (DP) and PPa co-loaded liposomes (L/DP&PPa). DP was synthesized to endow the good remote drug loading property of PR104A *via* introducing tertiary amine group[29]. Next, the biomimetic liposomes (PML/DP&PPa), also described as "platesomes", were fabricated by fusing platelet membranes with L/DP&PPa (Fig. 1). Under the intratumoral hemorrhage environment caused by CA4P, PML/DP&PPa showed high tumor accumulation by utilizing the magnified EPR effect as well as platelet-mimicking biological targeting. In addition, PPa-mediated PDT would consume oxygen, and the blocking of blood vessels by CA4P could further inhibit the restoration of oxygen supply to the tumor. The lasting and severe hypoxic TME were proactively constructed, which could not only maximize the activation of HAPs for hypoxia-selective chemotherapy, but also induce cell necrosis or apoptosis as well as inhibit tumor metastasis. Our findings pave the way for the artificial regulation of TME by CA4P-induced cascade processes of hemorrhage and shutdown, which could enhance platesomes' tumor distribution and promote synergistic photodynamic and hypoxia-selective therapy.

2. Materials and methods

2.1. Materials

Pyropheophorbide a (PPa) was purchased from Shanghai Xianhui Pharmaceutical Co., Ltd. (Shanghai, China). *N*,*N*-Dimethylglycine (DMG), *N*-methylmorpholine (NMM), 2-(7-azabenzotriazol-1-yl)-*N*,*N*,*N*′,*N*′-tetramethyluronium hexafluorophosphate (HATU) were purchased from J&K Scientific Co., Ltd. (Beijing, China). 1, 2-Distearoyl-*sn*-glycero-3-phosphocholine (DSPC), 1,2-distearoyl-*sn*-glycero-3-phosphoethanolamine-*N*-[methoxy(polyethylene glycol)-2000] (DSPE-mPEG$_{2k}$), cholesterol were obtained from Shanghai Advanced Vehicle Technology Co., Ltd. (Shanghai, China). Sepharose CL-4B, Coomassie Brilliant Blue Fast Staining solution and Hoechst 33342 were obtained from Solarbio Science & Technology Co., Ltd. (Beijing, China). The anti-P-selectin antibody (A1425), anti-CD61 antibody (A2542), anti-CD47 antibody (A1838), anti-CD31 antibody (A0378) and anti-Ki-67 antibody (A2094) were purchased from ABclonal Biotechnology Co., Ltd.

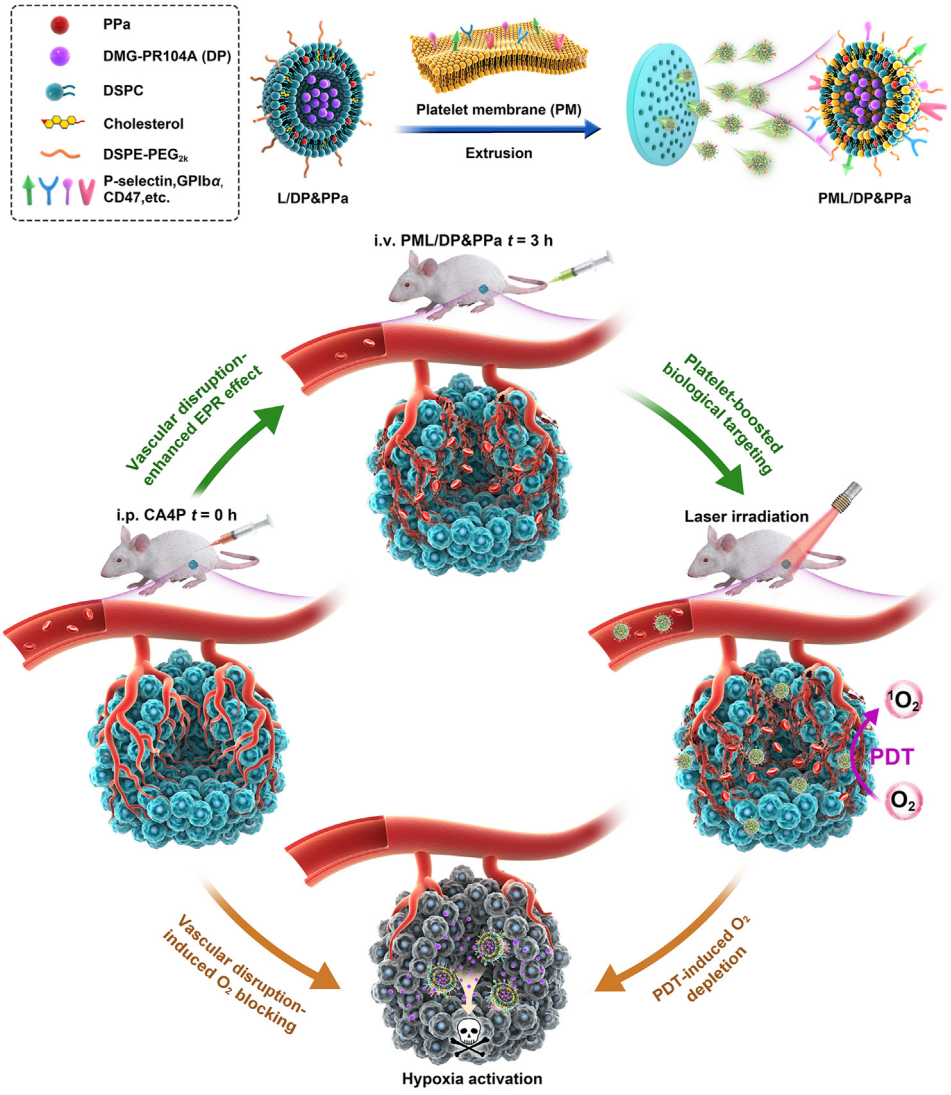

Figure 1 Schematic representation of the preparation of PPa and DP co-encapsulated platelet membrane fused biomimetic liposomes, and the underlying mechanism of the PML/DP&PPa combined with vascular disrupting agent CA4P to amplify the antitumor effects: (i) high tumor accumulation *via* damaged vessel-amplified EPR effect and platesomes-driven bio-targeting; (ii) synergistic-bioactivation of DP relied on CA4P-inhibited oxygen supply during occlusion and PDT-caused acute hypoxia.

(Wuhan, China). The anti-GPIbα antibody (bs-2347R) was obtained from Biosynthesis Biotechnology Inc. (Beijing, China). The anti-CD41 antibody (DF7456) and anti-HIF-1α antibody (AF1009) were purchased from Affinity Biosciences Ltd. (Cincinnati, OH, USA). Cell culture dishes/plates and 20 mm glass-bottom dishes were obtained from NEST Biotechnology Co., Ltd. (Wuxi, China).

2.2. *Synthesis and characterization of DMG-PR104A(DP)*

The synthesis of PR104A was based on our previous reports[26,30]. To synthesize DP, DMG (1 mmol/L), HATU (1.26 mmol/L), NMM (2.47 mmol/L) were stirred in anhydrous acetonitrile at 0 °C for 1 h PR104A (1.5 mmol/L) was subsequently joined in the above reaction system and kept reacting overnight at room temperature. The structure of DP was confirmed by both SolariX 7.0T ESI-MS (Bruker, Germany) and AV-400 NMR Spectroscopy (Bruker, Germany). HRMS (ESI) *m/z*: $[M + H]^+$ Calcd. for $C_{18}H_{27}BrN_5O_{10}S$, 584.066774; Found, 584.065652. ^{1}H NMR (600 MHz, $CDCl_3$) δ 8.62 (d, J = 2.8 Hz, 1H), 8.52 (d, J = 2.8 Hz, 1H), 7.96 (s, 1H), 4.41 (t, J = 5.0 Hz, 2H), 4.37 (t, J = 5.2 Hz, 2H), 3.77 (q, J = 5.4 Hz, 2H), 3.64-3.49 (m, 6H), 3.41 (s, 2H), 3.02 (s, 3H), 2.51 (s, 6H).

2.3. *Isolation of the platelet membrane*

The method of platelet membrane (PM) extraction was modified based on our previous study[11]. Briefly, fresh mouse blood adding sodium citrate was centrifuged at 200×*g* to separate platelet-rich plasma (PRP). Next, PRP was transferred into a new EP tube containing ACD (acid-citrate-dextrose) anticoagulant and centrifuged at 800×*g* to obtain the platelets. The collected platelets were suspended and ruptured in 0.25 × PBS solution at least 2 h at 4 °C, followed by centrifuging at 18,000×*g* for 15 min to obtain the isolated PM.

2.4. Preparation and characterization of platesomes

In brief, DSPC, cholesterol and DSPE-mPEG$_{2k}$ (3:1:0.05, *w*/*w*) were dispersed in chloroform followed by evaporation. The thin film was hydrated with 300 mmol/L ammonium sulfate and got blank liposomes after sonication. For preparing the PPa encapsulated liposome (L/PPa), the hydrophobic PPa was added with the membrane materials together. While making the DP encapsulated liposome (L/DP), an ammonium ion gradient was created by replacing the blank liposome's external phase (sucrose 300 mmol/L, HEPES buffer 20 mmol/L) through Sepharose CL-4B columns. DP was dissolved in ethanol and dropwise added under stirring at 65 °C for 20 min. The preparation of platelet membrane fusogenic liposomes (PML) referred to the methods previously reported[31]. In short, the PM and initial liposomes were further extruded through polycarbonate membrane by a mini-extruder (Avestin Inc., Ottawa, Canada) and purified using Sepharose CL-4B columns. Nano ZS Zetasizer instrument (Malvern Panalytical Ltd., Malvern, UK) and JEM100 CX II transmission electron microscope (TEM, JEOL Ltd., Mitaka, Japan) were used to characterize platesomes.

2.5. Membrane protein characterization

The quantified proteins could be separated with SDS-PAGE electrophoresis and gel imaging analysis was carried out using the Coomassie Brilliant Blue method. For Western blotting analysis, the transferred proteins were incubated with the primary antibodies overnight at 4 °C. Afterward, proteins were incubated with a secondary antibody for 1 h at room temperature. The ECL Western Blotting Substrate was added to the blotted films before the final visualization on ChemiDOC™ XRS+ (Bio-Rad Laboratories, Hercules, CA, USA).

For immunogold staining, the sample solution was dropped onto a carbon-coated copper grid, followed by blocking with PBS containing 1% BSA for 15 min. After 2 h treated with anti-CD61 antibody, the grid was washed three times with PBS and added gold conjugated secondary antibody to incubate for 1 h. Following PBS washing, the samples were fixed with 1% glutaraldehyde in PBS for 5 min and stained with 2% vanadium solution. Imaging was carried out using TEM.

2.6. Membrane fusogenic property

In the study of membrane colocalization, PML/DP&PPa was fabricated using the DiO-labeled PM vesicles and then observed under Confocal Laser Scanning Microscopy (CLSM, Nikon Corporation, Tokyo, Japan). A physical mixture of PM and L/DP&PPa was prepared as the control. The fusion of the lipid membrane and PM was further confirmed using a previously reported method[32]. The bare liposomes were labeled with a pair of fluorescent resonance energy transfer (FRET) dye DiO and DiI. The PM was co-extruded with the labeled liposomes at a different weight ratio of liposomes to PM proteins. The fluorescence spectrum of the dye-labeled PML was recorded from 490 to 630 nm *via* a microplate reader (BioTek Instruments Inc., Winooski, VT, USA) with an excitation wavelength at 450 nm.

2.7. In vitro stability and drug release

The colloidal stability of L/DP&PPa and PML/DP&PPa was monitored by incubating in pH 7.4 PBS containing 10% of FBS for 24 h at 37 °C. Furthermore, both were stored at 4 °C for 1 week to investigate the long-term stability. For *in vitro* DP release, nanoformulations were added into dialysis bags (10K MWCO) and suspended in PBS (pH 7.4) under gently shaken at 37 °C. At pre-determined time points, the concentration of DP was measured by HPLC.

2.8. In vitro ROS generation and O_2 consumption

The DPBF was dispersed in different samples at a PPa dose of 20 μg/mL. When exposed to 660 nm laser irradiation (100 mW/cm^2), the absorption was detected every 10 s to monitor singlet oxygen level. At initial and 5 min after irradiation, the dissolved O_2 in the above solution was measured using a JPB-607A portable dissolved oxygen meter (INASE Scientific Instrument Co., Ltd., Shanghai, China).

2.9. CD44 receptor expression

4T1 and 3T3 cells were harvested and resuspended at a density of 10^6 cells/tube. After centrifugation at 350×*g* for 5 min, cells were pre-incubated with a blocking buffer for 10 min on ice. Then cells were incubated with FITC anti-CD44 antibody or FITC CD44 isotype control antibody for 20 min. After rewashed with PBS, the cells were analyzed by flow cytometry (BD Biosciences, Franklin Lakes, NJ, USA).

2.10. Cell binding assay

4T1 and 3T3 cells were inoculated in 96-well plates and 20 mm glass-bottom dishes at a density of 2×10^4/well and 3×10^4 cells/dish. The DiD-labeled platelets were co-incubated with cells for 4 h (cell:platelet = 1:3000). After washing off the non-binding platelets, the cells were stained with Hoechst for 10 min before CLSM imaging (Nikon Corporation). The fluorescent intensity values were measured by a microplate reader (BioTek Instruments Inc.).

2.11. Collagen binding assay

According to the method established in references[9], the blank or collagen type IV coated 96-well black plates were pre-blocked with 2% BSA for 15 min. The L/DP&PPa and PML/DP&PPa (0.05 mg/mL equivalent PPa) were added for 2 min. Afterward, the plates were washed with PBS three times and fluorescence quantification was performed using a microplate reader (BioTek Instruments Inc.). In order to mimic the epithelial structure, mouse aortic epithelial cells (MAEC) were seeded in collagen-coated 96-well plates at a density of 3×10^4 cells/well for 12 h. Then, the medium was replaced by a fresh one with or without 100 μmol/L CA4P and incubated for another 8 h. L/DP&PPa and PML/DP&PPa were added at a PPa dose of 0.2 mg/mL for incubating 2 min, followed by rewashed with PBS. Retained formulations were then quantified by a microplate reader (BioTek Instruments Inc.).

2.12. Cellular uptake

4T1 and 3T3 cells were seeded in 24-well plates and 12-well plates at a density of 3×10^4 and 1×10^5 cells/well for 24 h, respectively. Then, the medium was replaced by free PPa,

L/DP&PPa, PML/DP&PPa and PML/DP&PPa+HA (6 mg/mL) contained culture medium (2 μmol/L equivalent PPa) and incubated for 4 h. The cellular uptake was observed and quantified by CLSM (Nikon Corporation) and flow cytometry (BD Biosciences).

2.13. Intracellular ROS/hypoxia detection

4T1 cells were seeded in 20 mm glass-bottom dishes or 12-well plates at a density of 1×10^5 cells for 24 h. The different groups (0.25 μmol/L equivalent PPa) were treated for 4 h at 37 °C. According to the ROS-ID® Hypoxia/Oxidative Stress Detection Kit (Enzo Life Sciences) instruction, ROS/Hypoxia probe was pre-incubated for 1 h before exposure 660 nm laser irradiation (0.5 min, 100 mW/cm^2). After rewashed with PBS, intracellular hypoxia and ROS analysis were performed by CLSM (Nikon Corporation) and flow cytometry (BD Biosciences).

2.14. Cytotoxicity assay

The cytotoxicity was evaluated by MTT viability assay. 4T1 cells or 3T3 cells were seeded into 96-well plates at a density of 2500 cells/well for 24 h. Then, the cells were treated with serial dilutions of free drug solutions or formulations for 24 h. The PPa-containing groups were received 660 nm laser irradiation (60 mW/cm^2, 0.5 min) at 4 h, followed by incubation for an additional 20 h. Besides, the cytotoxicity of free DP solution against 4T1 cells under hypoxia (20%) and normoxia (1%) conditions for 48h was further evaluated. The IC_{50} values were calculated by GraphPad Prism 7.

2.15. Animal studies

All experimental procedures were executed according to the protocols approved by Shenyang Pharmaceutical University Animal Care and Use Committee.

2.16. In vivo tumor vessel permeability assay

4T1 cells (100 μL; 5×10^6) were inoculated subcutaneously of female BALB/c mice to establish xenograft 4T1 tumor-bearing mice models. Mice bearing tumors of approximately 300 mm^3 were treated with CA4P (i.p. 100 mg/kg) solution or saline. Evans blue (40 mg/kg) was intravenously administrated to mice at predetermined time intervals. After 30 min, the external photographs of tumors were taken, and the mice were sacrificed to harvest tumors and the major organs. Evans blue was extracted and quantified by UV−Vis spectrophotometer (UV-1102II, Techcomp Instrument Co., Ltd., Shanghai, China). Tumor slices were observed by CLSM (Nikon Corporation).

In order to investigate the vascular permeability after repeated treatment of CA4P +PML/DP&PPa, the tumor-bearing mice were administrated three times according to the protocol of pharmacodynamics study under Section 2.20. The mice were randomly divided into two groups before the fourth dose, with three mice in each group. CA4P and saline were injected intraperitoneally and the tumor vascular permeability at 3 h was measured based on Evans blue method as above.

2.17. In vivo tumor hypoxia assay

The Hypoxyprobe™ Red549 Kit (Hypoxyprobe) was selected to assess hypoxia in different tissues. Mice bearing 4T1 tumors 300 mm^3 in volume were treated with saline, CA4P, PML/DP&PPa or CA4P+PML/DP&PPa (100 mg/kg CA4P; 1 mg/kg equivalent PPa). The CA4P was injected intraperitoneally, whereas the others were performed tail vein injection. Combination therapy groups always received CA4P 3 h before the other administrations. In the PPa-loaded group, the tumors underwent radiation with 660 nm NIR light (200 mW/cm^2, 5 min) at 24 h post-injection. After that, the mice were intraperitoneally injected with pimonidazole hydrochloride (60 mg/kg) and sacrificed 1.5 h later. Tumors were harvested and then embedded in OCT compound to get 10 μm thickness frozen sections. The tumor slices were treated as stated in the kit instruction and images were taken using CLSM (Nikon Corporation). The fluorescence intensity was quantitatively analyzed using the ImageJ.

2.18. In vivo pharmacokinetic study

Male Sprague–Dawley rats (220–250 g) were intravenously administrated with free PPa solution, L/DP&PPa and PML/DP&PPa at a dose of 1 mg/kg equivalent to PPa ($n = 5$). Blood samples were collected into heparin tubes at pre-determined time intervals after intravenous injection. The blood samples were centrifuged and the plasma concentrations of PPa were measured by a microplate reader (BioTek Instruments Inc.).

2.19. In vivo biodistribution

Biodistribution experiments were carried out on 4T1 xenograft bearing BALB/c mice. After the tumor volume was approximately 300 mm^3, PPa solution, PML/DP&PPa, CA4P+L/DP&PPa and CA4P+PML/DP&PPa were administered at an equivalent PPa dose of 2 mg/kg ($n = 3$). The administration sequence was the same as mentioned. The mice were sacrificed at 4 or 24 h post-injection. The fluorescence signals in normal tissues and tumors were detected using the IVIS® Lumina III Small Animal Imaging System (PerkinElmer Inc., Waltham, MA, USA). The platesomes' targeting mechanism *in vivo* was further analyzed *via* DAPI and CD31 immunofluorescence slices staining of the tumor harvested 24 h post-injection.

In order to investigate the tumor accumulation after repeated treatment of CA4P +PML/DP&PPa, the tumor-bearing mice were administrated three times according to the protocol of pharmacodynamics study under Section 2.20. The mice were randomly divided into two groups before the fourth dose, with three mice in each group. The mice were treated separately with PML/DP&PPa or CA4P+PML/DP&PPa as above. After 24 h post-injection, mice were sacrificed and the fluorescence signals in tumors were detected.

2.20. In vivo antitumor efficacy

Female BALB/c mice bearing xenograft or orthotopic 4T1 tumors, approximately 150 or 100 mm^3 in volume, were randomly divided into six groups ($n = 5$). Then, the mice were treated with saline, CA4P+DP+PPa sol, PML/DP&PPa, CA4P+PML/DP, CA4P+L/DP&PPa and CA4P+PML/DP&PPa at an equivalent DP dose of 8 mg/kg, PPa 0.5 mg/kg and CA4P 100 mg/kg on Days 0, 3, 6, and 9. The administration sequence and laser irradiation settings remained as above. Tumor volumes were measured every other day by digital calipers to assess the antitumor activities, and body weights were measured simultaneously to observe systemic toxicity. On Day 12, mice were sacrificed, the blood samples were centrifuged to obtain the serum for hepatorenal function analysis

(blood urea nitrogen (BUN), creatinine (CRE), serum aspartate aminotransferase (AST), alanine aminotransferase (ALT)). The tumor tissues and major organs were harvested. The lungs of 4T1 orthotopic breast tumor-bearing mice were fixed in Bouin's solution for 24 h followed by stored in 70% ethanol. The visible metastatic nodules were counted and analyzed.

Tumor tissues and major organs of mice were analyzed *via* hematoxylin and eosin (H&E) staining, immunofluorescence staining (*i.e.*, Tunel, Ki-67 and HIF-1α) and immunohistochemical staining (CD31). For the images of xenograft tumor slices, three randomly selected microscopic fields were quantified with ImageJ. The representative full scan images of orthotopic tumor slices were taken *via* Pannoramic MIDI (3DHISTECH Ltd., Hungary). These full scan images were observed by CaseViewer 2.2 and quantified *via* Image-Pro Plus 6.0 and ImageJ.

2.21. Statistical analysis

Data were presented as mean ± standard deviation (SD). Comparison between groups was analyzed with Student's *t*-test and one-way analysis of variance (ANOVA), and $P < 0.05$ was considered statistically significant.

3. Results and discussion

3.1. Preparation and characterization of PML/DP&PPa

As shown in Supporting Information Fig. S1, a weak-base pro-prodrug DP was successfully synthesized by conjugating PR104A and DMG with an ester bond, as confirmed by mass spectrum (MS) and ^{1}H NMR. The pro-prodrug DP could undergo rapid hydrolysis to release PR104A, as shown in Supporting Information Fig. S2. Bare liposomes were prepared using DSPC: cholesterol: DSPE-mPEG$_{2k}$ (3:1:0.05, *w*/*w*) by the conventional thin-film hydration technique. Hypoxia-activated DP and photosensitizers PPa were co-encapsulated in liposomes (L/DP&PPa) by active- and passive-loading methods, respectively. Based on the drug synergistic effect analyzed by the combination index (CI, Supporting Information Table S1), the drug loading ratio of the PPa and DP was selected as 1:20. The encapsulation efficiency of L/DP&PPa was found to be 82.3% for DP and 98.4% for PPa, respectively (Supporting Information Table S2). Due to the introduction of the tertiary amine group, the pro-prodrug DP could be remotely loaded into the interior aqueous phase of liposomes *via* an ammonium sulfate gradient.

To prepare biomimetic platesomes (PML/DP&PPa), the platelet membrane (PM) was separated after the rupture in the hypotonic medium and then was repeatedly coextruded with the prepared L/DP&PPa through polycarbonate membrane. As shown in Supporting Information Fig. S3, the hydrodynamic diameter of PML/DP&PPa increased with the platelet density. In order to ensure the fusogenic flexibility and narrow size distribution of platesomes, the optimal ratio of the formulation was selected (2.5×10^8 platelets:1 mg lipid) for further studies. Both L/DP&PPa and PML/DP&PPa had regular spherical structure and similar hydrodynamic diameters, much smaller than those of PM vesicles, extruded PM vesicles, the mixture of PM vesicles and L/DP&PPa (Fig. 2A and B and Table S2). After modification with PM, the average zeta potential of PML/DP&PPa was between L/DP&PPa and PM vesicles. These results further proved the successful preparation of biomimetic liposomes.

3.2. Protein characterization and membrane fusion verification of PML/DP&PPa

The protein profiles were determined by SDS-PAGE and the protein sequences of PM were well retained in PML/DP, PML/PPa, and PML/DP&PPa (Fig. 2D). A series of distinctive proteins on PM and platesomes were further confirmed by Western blotting, immunogold staining and TEM analysis. Several glycoprotein receptors on the platelet surface play a pivotal role in maintaining pro-coagulant activity[8,33]. For instance, as the binding receptor of collagen, the GPIb-IX-V complex composed of GPIbα and other platelet glycoproteins facilitates initial platelet adhesion on injured vascular endothelium with the involvement of von Willebrand factor. CD41 joins with CD61 to form integrin αIIbβ3, as a fibrinogen receptor, which participates in platelets' adhesion and aggregation during coagulation. Additionally, platelets are able to recognize tumor cells and evade immune surveillance by means of P-selectin and CD47 expression, respectively. As displayed in Fig. 2C and E, the successful preservation of platelets' crucial proteins on platesomes indicated that platesomes could have platelet-like functions.

To demonstrate the successful fusion of cell membranes and liposomes, PPa-labeled liposome membrane (red) and DiO-labeled PM (green) on PML/DP&PPa exhibited yellow fluorescence after the coextrusion process, whereas the physical mixture showed non-overlapping red and green fluorescence distribution (Fig. 2F). In addition, a fluorescent resonance energy transfer (FRET) study of DiO/DiI-labelled PM-fused liposomes was carried out[34]. As shown in Fig. 2G, the FRET peak (DiO excited, DiI emission observed) decreased while the donor (DiO) peak intensity increased due to the longer donor-acceptor distance caused by PM insertion into liposomes. Taken together, the biomimetic platesomes *via* membrane fusion were successfully prepared.

3.3. In vitro stability and release characteristics of PML/DP&PPa

The store stability (4 °C) and the colloidal stability (10% FBS, pH 7.4) of both PML/DP&PPa and L/DP&PPa were excellent, as shown in Supporting Information Fig. S4. The absorbance spectra showed that the characteristic peaks of PPa and DP were observed in PML/DP&PPa and L/DP&PPa (Fig. 2H), indicating the successful encapsulation of PPa and DP. Moreover, the *in vitro* release profiles of DP from PML/DP&PPa and L/DP&PPa were determined. About 39% of DP was released from PML/DP&PPa and approximately 45% of DP was released from L/DP&PPa within 12 h, suggesting that the membrane fusion did not influence the liposomal sustained-release properties (Fig. 2I).

3.4. In vitro tumor-targeting ability

P-selectin is a cell adhesion molecule expressed both on platelets and platesomes. CD44 is usually overexpressed on the surface of tumor cells. Current reports showed that P-selectin-mediated platelets adhesion to CD44-overexpressed tumor cells heavily promotes cancer metastasis and results in poor prognosis[9,35]. We have found that mouse breast cancer 4T1 cells exhibited higher CD44 expression than mouse embryonic fibroblast 3T3 cells (Supporting Information Fig. S5). Thus, as a representative of cancerous and normal cell lines, 4T1 and 3T3 cells were selected to evaluate the targeting capability of platelets and platesomes. When the two cell lines were treated with DiD-labeled platelets

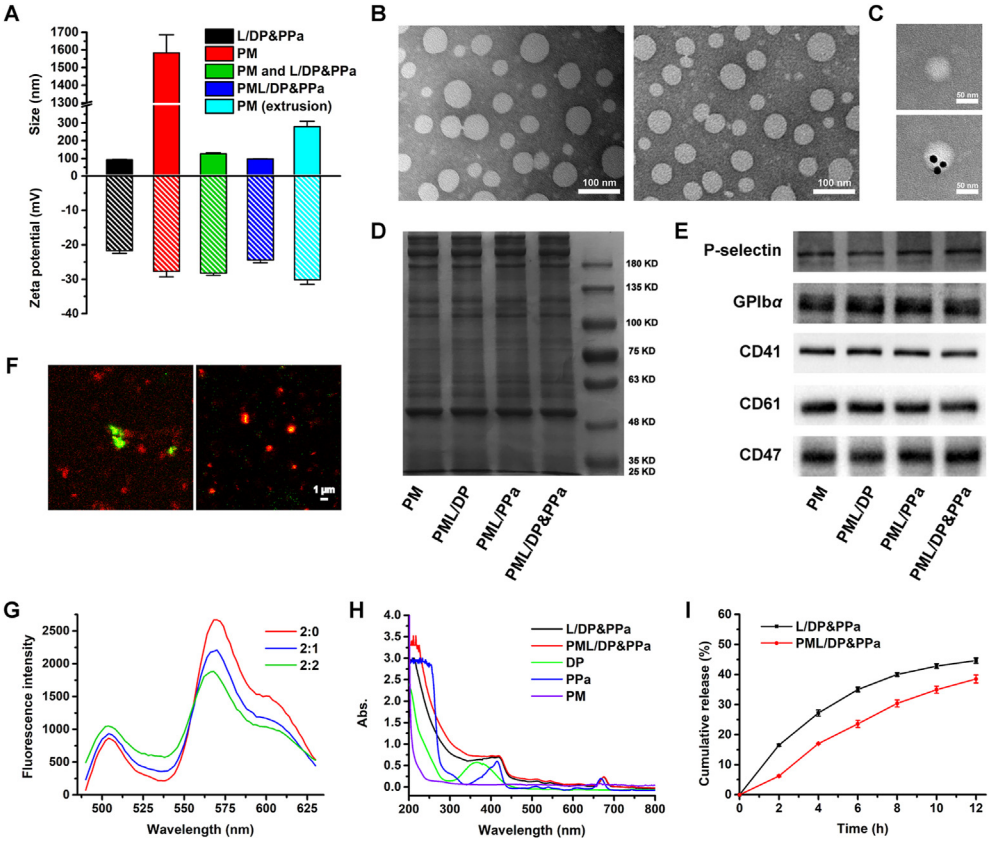

Figure 2 Characterization of PML/DP&PPa. (A) Size distribution and zeta potential measured by DLS. (B) TEM images of L/DP&PPa (left) and PML/DP&PPa (right). (C) TEM images of L/DP&PPa (upper) and PML/DP&PPa (lower) with CD61 stained by immunogold labeling. (D) SDS-PAGE protein tracking. (E) Western blotting analysis of the characteristic platelet markers (P-selectin, GPIbα, CD41, CD61, and CD47). (F) CLSM images of PML/DP&PPa (right) and the physical mixture of PM vesicles and L/DP&PPa (left). Red: liposomes; green: PM vesicles. (G) A pair of FRET fluorescent dyes DiI/DiO-labelled liposomes were fused with increasing amounts of PM vesicles, and the emission spectra were recorded. The ratio indicated the weight ratio of liposomes to PM proteins. (H) Absorbance spectra of L/DP&PPa, PML/DP&PPa, DP, PPa and PM. (I) *In vitro* DP release of L/DP&PPa and PML/DP&PPa in PBS at 37 °C. Data are presented as mean ± SD ($n = 3$).

for 4 h, confocal images and quantitative analysis in Supporting Information Fig. S6 showed higher red fluorescence intensity in 4T1 cells than 3T3 cells, demonstrating that platelets had a higher affinity to CD44-overexpressed 4T1 cells.

Furthermore, 4T1 and 3T3 cells were incubated with free PPa solution, L/DP&PPa and PML/DP&PPa for 4 h to investigate cellular uptake. Compared with 3T3 cells, about 1.86-fold higher fluorescence was observed on 4T1 cells treated with PML/DP&PPa (Fig. 3A and B), whereas there was little difference in the fluorescence intensity of 4T1 cells treated with L/DP&PPa or free PPa. The uptake efficiency of PML/DP&PPa was reduced by nearly 60% when co-incubated with hyaluronan (HA), a competitive CD44 ligand. These results proved that the biomimetic platesomes had a selective targeting effect on cancerous 4T1 cells mainly *via* specific interaction between platesomes' P-selectin and CD44 on tumor cells.

3.5. *In vitro collagen-binding ability*

In view of the inherent collagen adhesion properties of platelets, the collagen-binding ability of platesomes *in vitro* was studied. As a primary subendothelial component, type IV collagen was coated on the plates before adding different formulations. As displayed in Fig. 3E, compared with non-collagen-coated plates, platelet membrane-camouflaged PML/DP&PPa adhered on the collagen-coated plate increased significantly, while the retention of L/DP&PPa was rarely whether the plate coated with collagen or not. This suggests that the biomimetic platesomes successfully inherited the collagen-binding functionality of platelets.

To further investigate the effect of CA4P on platesome adhesion, the model of endothelial cells MAEC seeded on collagen-coated culture plates was used to simulate the vascular endothelial structure. Fluorescence quantitative result (Fig. 3F) showed that stronger intensity of fluorescence appeared in CA4P+PML/DP&PPa among four groups. This is possibly caused by the exposure of the basement membrane after the rapid morphological changes of the endothelial cells, that is, CA4P provide opportunities for the adhesion of the platesomes with collagen.

3.6. *Effects of CA4P on tumor vessel permeability*

The disruption effect of CA4P on tumor vascular integrity was evaluated using the dye Evans blue. Since Evans blue immediately forms approximately 10 nm Evans blue-albumin conjugate in blood, this macromolecular dye could only leak into the tissue with the injured vasculatures[36]. After intraperitoneal injection of CA4P, the highest tumoral Evans blue content was observed at 3 h, attributable to the enhanced permeability at the early stage of

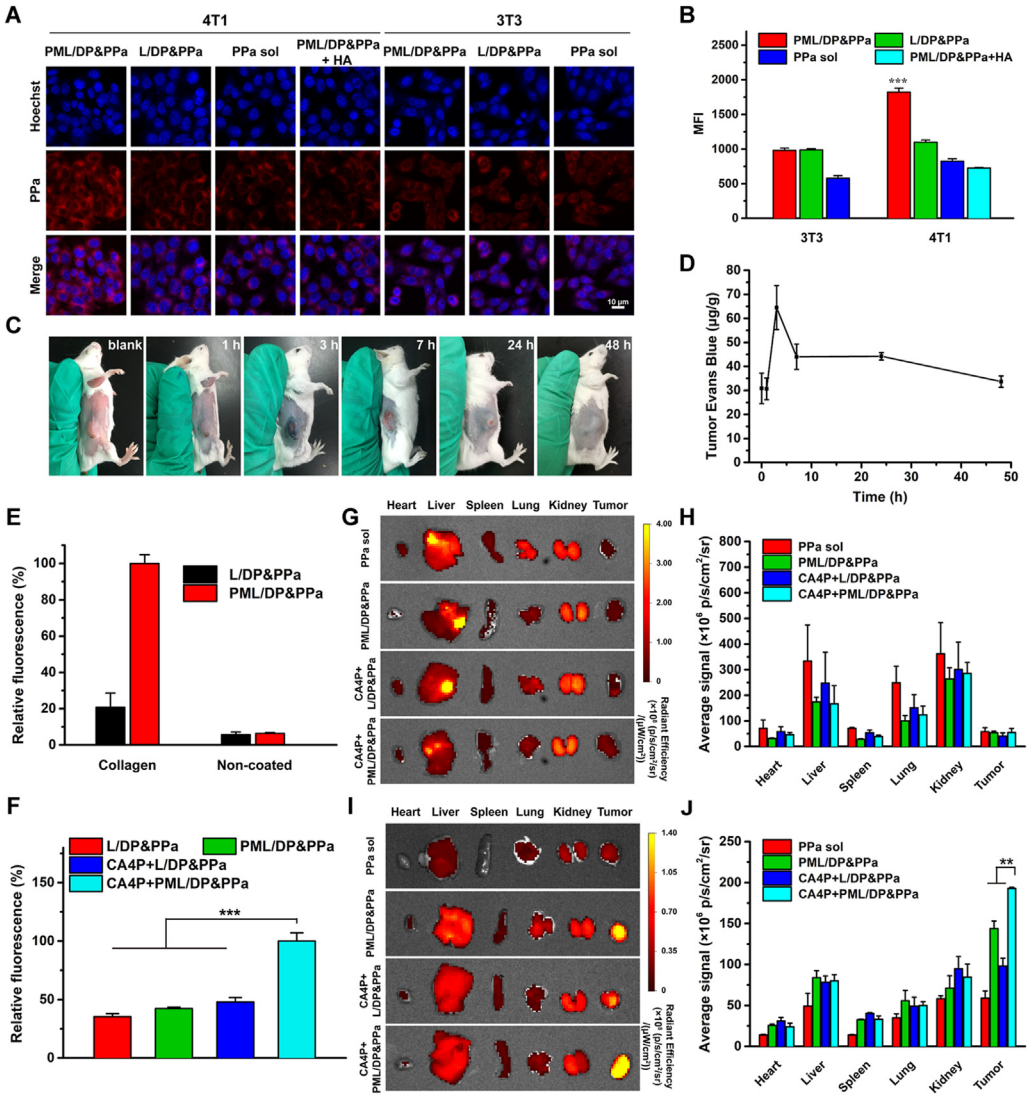

Figure 3 Co-promoted tumor targeting and accumulation. (A) CLSM images and (B) flow cytometry of 4T1 and 3T3 cells treated with free PPa, L/DP&PPa, PML/DP&PPa or PML/DP&PPa+HA for 4 h. (C) The photographs of the 4T1 tumor-bearing mice after intraperitoneal administration with CA4P (100 mg/kg) for 1, 3, 7, 24 and 48 h. (D) The tumor permeability of tumor-bearing mice changes over time after CA4P treatment. (E) Fluorescent quantification of L/DP&PPa or PML/DP&PPa bound to collagen-coated or non-coated plates. (F) Fluorescent quantification of L/DP&PPa and PML/DP&PPa (with the help of CA4P or not) adhesion on collagen-coated plates seeded with MAEC. *Ex vivo* distribution of PPa solution and different formulations at (G, H) 4 h and (I, J) 24 h. Data are presented as mean ± SD ($n = 3$). $^{**}P < 0.01$, $^{***}P < 0.001$.

tumor vessel collapse (Fig. 3C and D). Subsequently, the tumor infiltration of Evans blue gradually decreased based on the vascular occlusion along with coagulation and vessel remodeling, and finally returned to the normalized level within 48 h. Additionally, it was confirmed that the destruction of blood vessel integrity only occurred in tumor tissues but not in normal tissues (Supporting Information Fig. S7). The above results verified that CA4P-mediated vascular collapse and hemorrhage could selectively enhance the permeability of tumor blood vessels and then amplify the EPR effect.

3.7. *In vivo enhanced tumor targeting and accumulation profiles*

According to pharmacokinetic behavior shown in Supporting Information Fig. S8 and Table S3, the prolonged circulation and slower plasma clearance properties of liposomes might contribute to tumor accumulation. In order to validate whether CA4P and platelet-camouflaged method could synergistically promote tumor-specific targeting and accumulation, the biodistribution of PML/DP&PPa and L/DP&PPa with or without CA4P was evaluated in 4T1 xenograft tumor-bearing mice. As shown in Fig. 3G–J, PPa solution had non-selective systemic distribution, followed by rapid clearance at 24 h post-injection. Among them, the strongest tumor fluorescence signal could be observed in the sequential administration of CA4P and PML/DP&PPa. It highlighted the combination advantage of artificially-adjusted TME and biological targeting nanovehicles to overcome tumoral drug delivery obstacles.

In addition, the targeting behavior of platesomes *in vivo* was further investigated. As shown in Supporting Information Fig. S9,

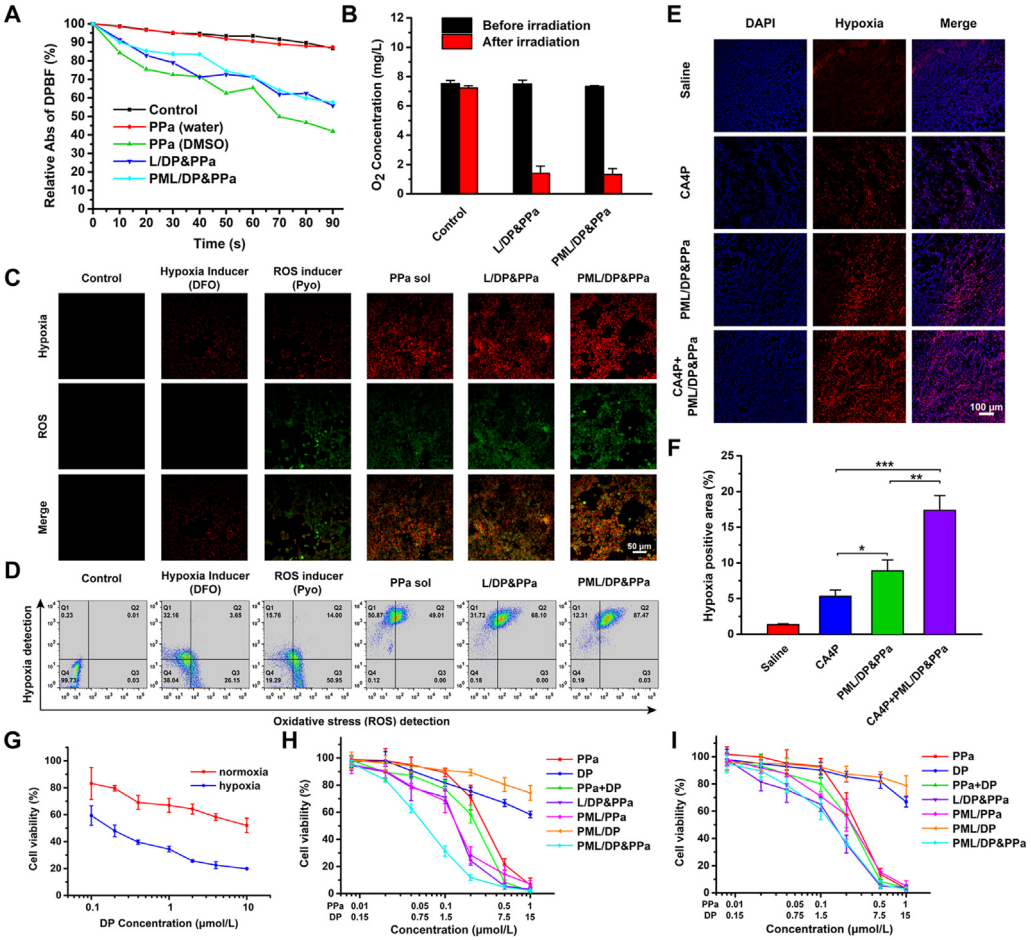

Figure 4 Co-aggravated tumor hypoxia for synergistic-bioactivation of HAP. (A) *In vitro* ROS generation under laser irradiation (100 mW/cm^2). (B) Measurement of O_2 concentration at 0 min and 5 min after laser irradiation (100 mW/cm^2). (C) CLSM images and (D) flow cytometry of 4T1 cells stained with ROS/hypoxia detection probes after laser irradiation (100 mW/cm^2, 0.5 min). (E) Hypoxia immunofluorescence staining images of tumor slices of mice treated by laser irradiation (200 mW/cm^2, 5 min) after 24 h tumor accumulation. (F) Quantitative analysis of hypoxia in tumor tissues. (G) Cytotoxicity of 4T1 cells incubated with free DP at various concentrations under normoxia or hypoxia for 48 h. Cytotoxicity of (H) 4T1 cells or (I) 3T3 cells under laser irradiation (60 mW/cm^2) for 0.5 min after different treatments for 24 h. Data are presented as mean ± SD ($n = 3$). *$P < 0.05$, **$P < 0.01$, ***$P < 0.001$.

the tumor treated with CA4P+PML/DP&PPa exhibited the strongest yellow and purple fluorescence, which was separately caused by the overlap fluorescence of the drug (red) and the vascular (green) or the drug (red) and the tumor cells (blue). It indicated that the PML/DP&PPa could actively target tumor cells and damaged tumor blood vessels *in vivo*, consistent with its targeting ability *in vitro*. In contrast, PML/DP&PPa alone showed almost no yellow fluorescence, proving that the platesomes' targeting to damaged vessels was based on the exposed collagen induced by CA4P.

3.8. *In vitro ROS generation and aggravated hypoxia*

Upon exposure to laser irradiation, photosensitizers would produce reactive oxygen species (ROS), such as singlet oxygen[37]. Based on DPBF's attenuated absorbance after interacting with singlet oxygen, we selected DPBF as a singlet oxygen probe to investigate the ROS generation capability of L/DP&PPa and PML/DP&PPa (Fig. 4A). Upon laser irradiation, UV absorption of DPBF in L/DP&PPa and PML/DP&PPa was reduced rapidly, similar to a PPa DMSO solution, indicating the significant production of ROS. When PPa was entrapped in the liposome membrane to prevent aggregation, liposomal PPa was endowed with a high-efficiency PDT property[38,39]. Furthermore, the oxygen concentration before and after laser irradiation was also measured (Fig. 4B). The results showed that L/DP&PPa and PML/DP&PPa could effectively aggravate hypoxia through photodynamic therapy.

In order to further evaluate the ability of intracellular ROS generation and O_2 consumption, 4T1 cells were irradiated after 4 h incubation with various nanoformulations. As shown in Fig. 4C, all groups showed prominent green (ROS) and red (hypoxia) fluorescences under laser irradiation, except for the negative control. Under laser irradiation, the capability of producing intracellular ROS generation followed the order of PML/DP&PPa> L/DP&PPa> free PPa. Collecting cells for flow cytometric analysis revealed that 87.47% of cells were sorted to the third quadrant after PML/DP&PPa treatment in Fig. 4D. PML/DP&PPa could induce more cells with high oxidative stress levels, mainly depending on its good tumor cell uptake efficiency as well as PPa dispersion molecular state on platesomes. Moreover, PML/DP&PPa could also cause severe intracellular hypoxia due to the highest ROS generation capacity under laser irradiation.

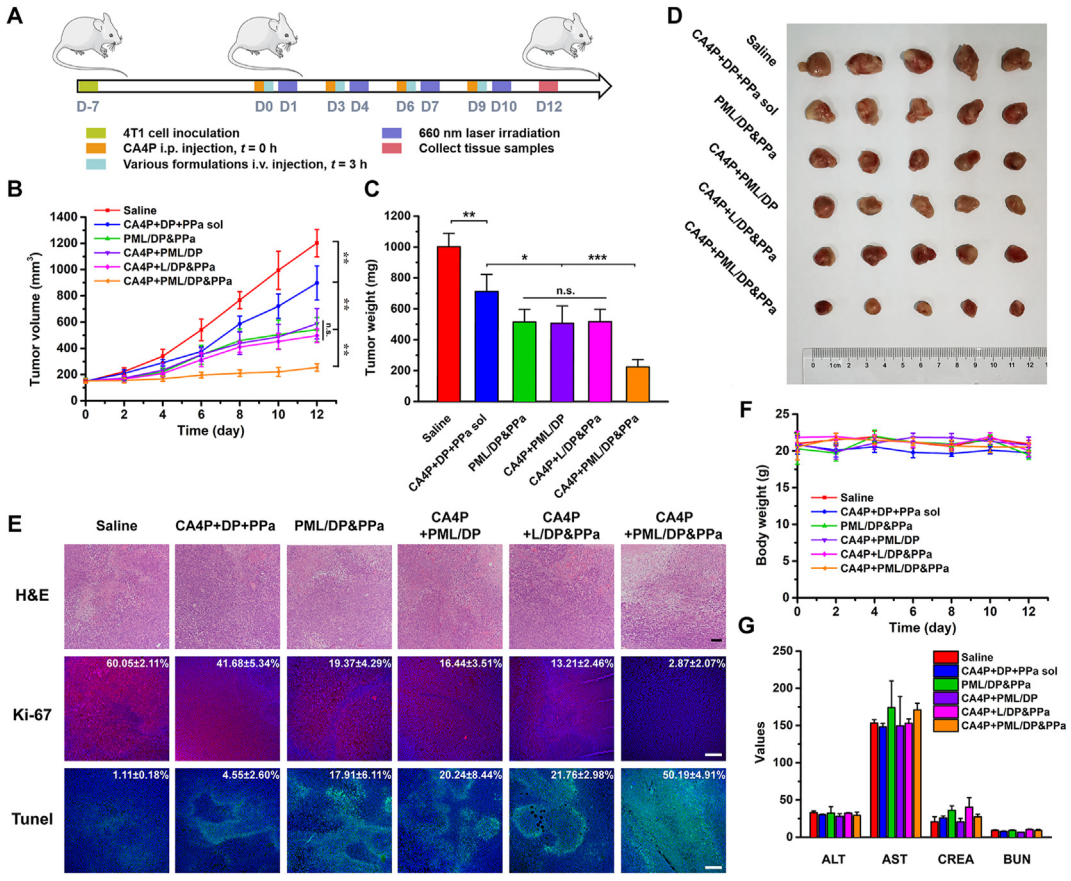

Figure 5 *In vivo* therapeutic efficacy of CA4P plus PML/DP&PPa against 4T1 xenograft tumors. (A) Pharmacodynamics study protocol. (B) Tumor growth profiles after treatment with different formulations. (C) Tumor weight and (D) tumor images at the end of the experiment. (E) Representative images of H&E, Ki-67, and Tunel staining of tumor sections. Scale bar: 100 μm. (F) Body weight changes of tumor-bearing mice during the treatment. (G) Serum biochemical marker analysis ($n = 3$). ALT (U/L): alanine aminotransferase; AST (U/L): aspartate aminotransferase; CREA (μmol/L): creatinine; BUN (mmol/L): blood urea nitrogen. Data are presented as mean ± SD ($n = 5$); $^{*}P < 0.05$, $^{**}P < 0.01$, $^{***}P < 0.001$; n.s., no significant difference.

3.9. *In vivo magnified tumor hypoxia detection*

The effects of CA4P and PML/DP&PPa on facilitating tumor hypoxia were investigated in 4T1 subcutaneous xenograft tumors *in vivo* (Fig. 4E and F). After 660 nm laser irradiation (200 mW/cm^2, 5 min) at 24 h post-injection, the tumor and normal tissues were collected for staining with a hypoxia probe. Confocal images and quantitative analysis results of hypoxia levels showed that strong tumor hypoxia fluorescence could be observed using CA4P or PML/DP&PPa alone, but it was almost undetectable in the saline group. If CA4P treatment was performed 3 h before the PML/DP&PPa administration, the most severe tumor hypoxia could be observed with the "depletion and blocking" parallel strategy. CA4P-induced vascular rupture blocked oxygen supply, and PPa-mediated PDT caused the further aggravation of hypoxia. It was worth noting that the enhanced hypoxia level could be found only in tumors but not in normal tissues, enabling good safety of CA4P plus PML/DP&PPa (Supporting Information Fig. S10).

3.10. *Hypoxia-activated cytotoxicity assay*

As a pro-prodrug, DP firstly released prodrug PR104A by ester hydrolysis. Subsequently, PR104A could be converted into the activated nitrogen mustard under hypoxic conditions, thereby causing cytotoxicity. The cytotoxicity of DP in 4T1 cells was investigated with an MTT assay. As shown in Fig. 4G and Supporting Information Table S4, the cytotoxicity of DP was significantly enhanced under hypoxic conditions than normoxia. Because of effective bioactivation under hypoxia, DP had an outstanding safety with hypoxia-dependent toxicity.

The cell-killing activity of free drug and nanoformulations was further evaluated in 4T1 and 3T3 cells. The half-maximal inhibitory concentration (IC_{50}) values were summarized in Supporting Information Table S5. According to Fig. 4H and I, PML/DP&PPa exhibited higher cytotoxicity than PML/DP or PML/PPa owing to the synergistic effect of PPa and DP. Moreover, compared to L/DP&PPa or the free combos (PPa+DP), the cytotoxicity of PML/DP&PPa was improved only against 4T1 cells, whereas there is no difference in 3T3 cells. Thus, platesomes had higher selective cytotoxicity against tumor cells by virtue of their efficient tumor cell uptake. It is worth noting that CA4P could also selectively kill 4T1 tumor cells rather than 3T3 cells (Supporting Information Fig. S11), indicating that the combination of CA4P and platesomes might boost the antitumor effect as well as well tolerated *in vivo*.

3.11. *In vivo antitumor efficacy of CA4P plus PML/DP&PPa*

In vivo combined antitumor effect of CA4P plus PML/DP&PPa was evaluated in 4T1 xenograft tumor-bearing mice. The dosage

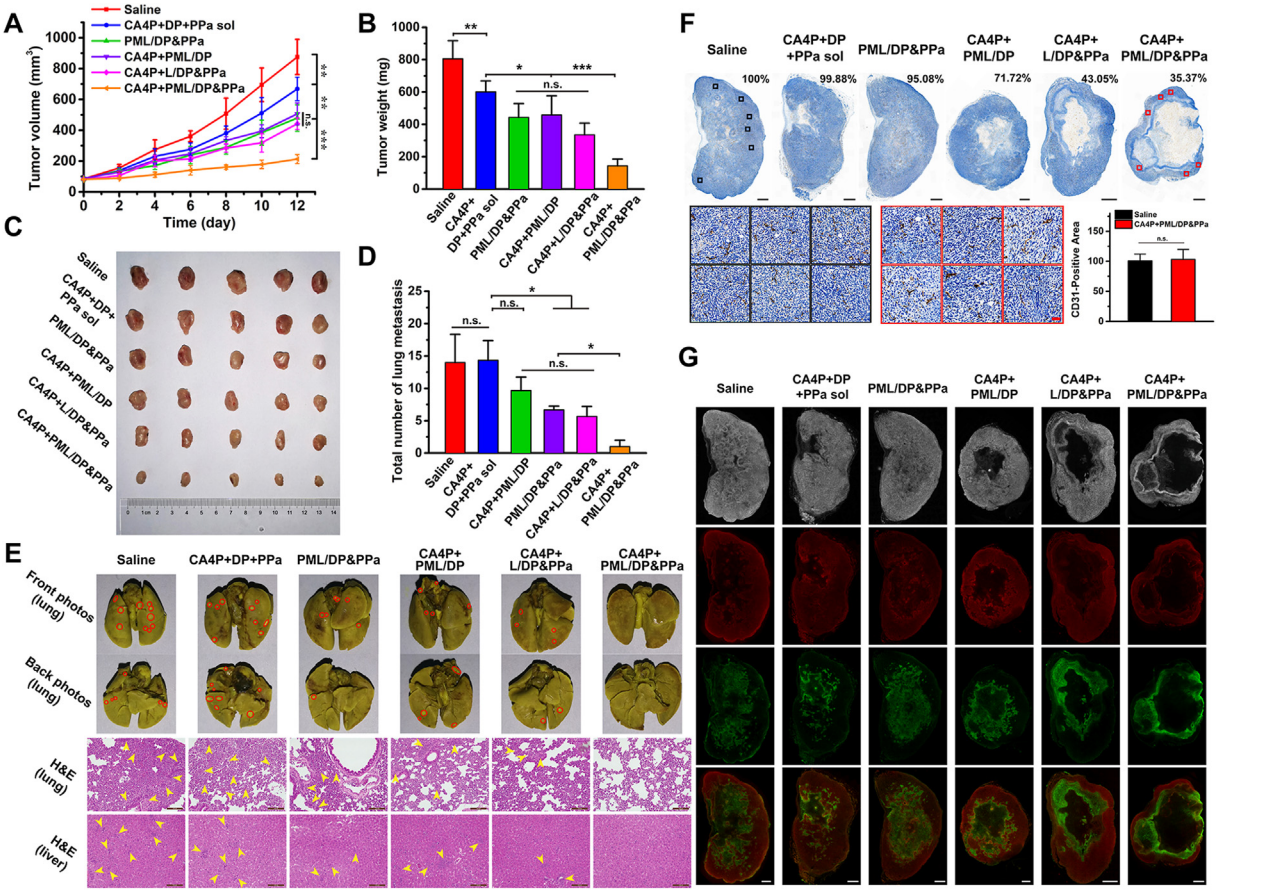

Figure 6 *In vivo* antimetastatic capacity of CA4P plus PML/DP&PPa against orthotopic 4T1 tumors. (A) Tumor growth profiles after treatment with different formulations. (B) Tumor weight and (C) tumor images at the end of the experiment. (D) Quantification of lung visible metastatic nodules ($n = 3$). (E) Representative photos of the whole lungs stained with Bouin's Fluid and H&E staining of the lung and liver. The red circles indicate the visible metastatic site. The yellow arrows demonstrate metastases in the lung and liver slices. Scale bar: 100 μm. (F) CD31 distribution in the representative full scan images of tumor slices (Top row, scale bar: 1 mm; Relative vessel density shown in right corner) and the magnified images delimited in tumor surviving regions (Bottom row, scale bar: 50 μm; Quantification of CD31 shown on the right, $n = 6$). (G) Representative bright field and fluorescence full scan images of tumor slices stained with HIF-1α (red) and Tunel assay (green). Scale bar: 1 mm. Data are presented as mean ± SD ($n = 5$); $^*P < 0.05$, $^{**}P < 0.01$, $^{***}P < 0.001$; n.s., no significant difference.

regimen was presented in Fig. 5A, and the photodynamic groups received laser irradiation (200 mW/cm^2) for 5 min at 24 h post-injection. Fig. 5B–D shows that tumors rapidly proliferated in the saline control group within 12 days. The mixed free drug (CA4P, DP, and PPa) solution exhibited an inferior antitumor effect owing to the unsatisfied drug delivery efficiency. PML/DP&PPa, CA4P+PML/DP, and CA4P+L/DP&PPa were able to inhibit the tumor growth to some extent than that of free drug combos, but there was no significant difference among the three groups. Notably, CA4P+PML/DP&PPa group significantly delayed tumor progression, exhibiting the best efficacy.

The pathological variation, proliferation and apoptosis in tumors were investigated *via* H&E staining and immunofluorescence staining. As shown in Fig. 5E, the negligible proliferation, widespread karyolysis and massive apoptosis areas were found in tumor sections of the CA4P+PML/DP&PPa group, consistent with the above results. The antitumor effect of CA4P+PML/DP&PPa might benefit from two advantages: (i) high intratumoral accumulation by virtue of CA4P-enhanced tumor permeability and platesomes-specific targeting to the hemorrhagic tumor; (ii) aggravated tumor hypoxia relied on a two-parallel approach of "obstruction and consumption" oxygen to trigger hypoxia-selective therapy. Besides, there were no significant changes in body weight and hematological parameters in each group (Fig. 5F and G). Thus, CA4P plus PML/DP&PPa was well tolerated with no noticeable side effects.

3.12. *In vivo antimetastatic ability of CA4P plus PML/DP&PPa*

Consistent with the xenograft tumor model results, a similar tumor suppression trend with good biosafety of each group was found in the metastatic orthotopic models in Fig. 6A–C and Supporting Information Figs. S12–S14. According to the full scan images of tumor slices in Fig. 6F, a significant reduction of intratumoral microvessel density was observed after repeated treatment of CA4P+PML/DP&PPa, as 35.37% compared with that of the saline control group. However, due to the heterogeneous distribution of vessels in tumor, there was no difference in microvessel density of the survival tumor area after repeated administration CA4P+PML/DP&PPa or saline.

In addition, as shown in Supporting Information Fig. S15, the increased degree of tumor vascular permeability and tumor

accumulation of the platesomes after repeated administration of the combined CA4P+PML/DP&PPa group showed the same trend as that of a single administration. Therefore, each CA4P+PML/DP&PPa administration could be able to damage vessels in tumor surviving regions, achieving enhanced tumor delivery efficiency and preferable antitumor effect.

Additionally, the lung and liver tissues of the 4T1 orthotopic tumor-bearing mice were processed and observed after the pharmacodynamic study. As displayed in Fig. 6D and E, there was nearly no evident tumor metastasis in CA4P+PML/DP&PPa treated group. In order to further explore its antimetastatic mechanism, immunofluorescence staining of hypoxia-inducible factor-1α (HIF-1α) and Tunel was observed through the full scan photos of maximum tumor cross-section. As shown in Fig. 6G, the residual tumor tissues of the CA4P+PML/DP&PPa group presented the largest central core necrosis and peripheral apoptosis region due to synergistic chemo-photodynamic therapy as well as severe and prolonged tumor hypoxia. As a critical pro-metastasis factor with specifically activated characteristics under hypoxia, HIF-1α was observed mainly in the peripheral survival tumor area[40,41]. Because of the largest proportion of dead cells, the expression of HIF-1α was lowest in CA4P+PML/DP&PPa-treated tumor (Supporting Information Fig. S16), which might be an important factor for effectively mitigating the risk of tumor metastasis.

4. Conclusions

Here, we emphasize that rationally remodeling TME can improve nano-drug delivery systems for effective cancer treatment. Aiming at the characteristics of tumor hemorrhage and vascular occlusion caused by CA4P, we prepared hypoxia-activated pro-prodrug DP and photosensitizer PPa co-loaded biomimetic platesomes (PML/DP&PPa) and intravenously injected it after intraperitoneal injection with CA4P for 3 h. Both the tumor bleeding enhanced-EPR effect and the platelet-mimicking biological targeting could make up for the low tumoral delivery efficiency of liposomes. Additionally, CA4P blocked the tumor's oxygen supply, further aggravating the tumor hypoxia caused by PDT. The prolonged severe hypoxia was able to effectively promote the activation of the hypoxia-activated pro-prodrug DP, thereby significantly inhibiting tumor growth and metastasis. Our findings provide new insights for the rational combination of vascular disrupting agents with platesomes for favorable tumor targeting and synergistic photodynamic and hypoxia-activated therapy.

Acknowledgments

This work was financially supported by the National Natural Science Foundation of China (No. 81773656), Liaoning Revitalization Talents Program (No. XLYC1808017, China), Shenyang Youth Science and Technology Innovation Talents Program (No. RC190454, China), College Student Innovation and Entrepreneurship Training Program of Shenyang Pharmaceutical University (No. X202010163141, China).

Author contributions

Jin Sun, Wenhui Tao and Dongyang Zhao designed the research. Wenhui Tao carried out the experiments and performed data analysis. Guanting Li, Lingxiao Li, Songhao Li, Hao Ye, Chutong Tian, Yutong Lu and Shuying Li participated part of the experiments. Zhonggui He and Yinghua Sun provided experimental drugs and quality control. Wenhui Tao and Dongyang Zhao wrote the manuscript. Jin Sun revised the manuscript. All of the authors have read and approved the final manuscript.

Conflicts of interest

The authors have no conflicts of interest to declare.

Appendix A. Supporting information

Supporting data to this article can be found online at https://doi.org/10.1016/j.apsb.2021.08.010.

References

1. Shi J, Kantoff PW, Wooster R, Farokhzad OC. Cancer nanomedicine: progress, challenges and opportunities. *Nat Rev Cancer* 2017;**17**:20−37.
2. Fang J, Nakamura H, Maeda H. The EPR effect: unique features of tumor blood vessels for drug delivery, factors involved, and limitations and augmentation of the effect. *Adv Drug Deliv Rev* 2011;**63**:136−51.
3. Sun D, Zhou S, Gao W. What went wrong with anticancer nanomedicine design and how to make it right. *ACS Nano* 2020;**14**:12281−90.
4. Danhier F. To exploit the tumor microenvironment: since the EPR effect fails in the clinic, what is the future of nanomedicine?. *J Control Release* 2016;**244**:108−21.
5. Chen Z, Hu Q, Gu Z. Leveraging engineering of cells for drug delivery. *Acc Chem Res* 2018;**51**:668−77.
6. Li R, He Y, Zhang S, Qin J, Wang J. Cell membrane-based nanoparticles: a new biomimetic platform for tumor diagnosis and treatment. *Acta Pharm Sin B* 2018;**8**:14−22.
7. Dhaliwal A, Zheng G. Improving accessibility of EPR-insensitive tumor phenotypes using EPR-adaptive strategies: designing a new perspective in nanomedicine delivery. *Theranostics* 2019;**9**:8091−108.
8. Hu Q, Sun W, Qian C, Wang C, Bomba HN, Gu Z. Anticancer platelet-mimicking nanovehicles. *Adv Mater* 2015;**27**:7043−50.
9. Hu CMJ, Fang RH, Wang KC, Luk BT, Thamphiwatana S, Dehaini D, et al. Nanoparticle biointerfacing by platelet membrane cloaking. *Nature* 2015;**526**:118−21.
10. Ye H, Wang K, Lu Q, Zhao J, Wang M, Kan Q, et al. Nanosponges of circulating tumor-derived exosomes for breast cancer metastasis inhibition. *Biomaterials* 2020;**242**:119932.
11. Ye H, Wang K, Wang M, Liu R, Song H, Li N, et al. Bioinspired nanoplatelets for chemo-photothermal therapy of breast cancer metastasis inhibition. *Biomaterials* 2019;**206**:1−12.
12. Zhou Y, Chen X, Cao J, Gao H. Overcoming the biological barriers in the tumor microenvironment for improving drug delivery and efficacy. *J Mater Chem B* 2020;**8**:6765−81.
13. Yang S, Gao H. Nanoparticles for modulating tumor microenvironment to improve drug delivery and tumor therapy. *Pharmacol Res* 2017;**126**:97−108.
14. Zhang W, Wang F, Hu C, Zhou Y, Gao H, Hu J. The progress and perspective of nanoparticle-enabled tumor metastasis treatment. *Acta Pharm Sin B* 2020;**10**:2037−53.
15. Dark GG, Hill SA, Prise VE, Tozer GM, Pettit GR, Chaplin DJ. Combretastatin A-4, an agent that displays potent and selective toxicity toward tumor vasculature. *Cancer Res* 1997;**57**:1829−34.
16. Tozer GM, Kanthou C, Parkins CS, Hill SA. The biology of the combretastatins as tumour vasculartargeting agents. *Int J Exp Pathol* 2002;**83**:21−38.
17. Tozer GM, Prise VE, Wilson J, Cemazar M, Shan S, Dewhirst MW. Mechanisms associated with tumor vascular shut-down induced by

combretastatin A-4 phosphate: intravital microscopy and measurement of vascular permeability. *Cancer Res* 2001;**61**:6413−22.
18. Satterlee AB, Rojas JD, Dayton PA, Huang L. Enhancing nanoparticle accumulation and retention in desmoplastic tumors *via* vascular disruption for internal radiation therapy. *Theranostics* 2017;**7**:253−69.
19. Volz J, Mammadova-Bach E, Gil-Pulido J, Nandigama R, Remer K, Sorokin L, et al. Inhibition of platelet GPVI induces intratumor hemorrhage and increases efficacy of chemotherapy in mice. *Blood* 2019;**133**:2696−706.
20. Song W, Tang Z, Zhang D, Li M, Gu J, Chen X. A cooperative polymeric platform for tumor-targeted drug delivery. *Chem Sci* 2016;**7**:728−36.
21. Carmeliet P, Jain RK. Principles and mechanisms of vessel normalization for cancer and other angiogenic diseases. *Nat Rev Drug Discov* 2011;**10**:417−27.
22. Brown JM, Wilson WR. Exploiting tumour hypoxia in cancer treatment. *Nat Rev Cancer* 2004;**4**:437−47.
23. Sharma A, Arambula JF, Koo S, Kumar R, Singh H, Sessler JL, et al. Hypoxia-targeted drug delivery. *Chem Soc Rev* 2019;**48**:771−813.
24. Kling J. Hypoxia-activated prodrugs forge ahead in cancer. *Nat Biotechnol* 2012;**30**:381.
25. Wilson WR, Hay MP. Targeting hypoxia in cancer therapy. *Nat Rev Cancer* 2011;**11**:393−410.
26. Zhao D, Tao W, Li S, Li L, Sun Y, Li G, et al. Light-triggered dual-modality drug release of self-assembled prodrug-nanoparticles for synergistic photodynamic and hypoxia-activated therapy. *Nanoscale Horiz* 2020;**5**:886−94.
27. Zhang L, Wang Z, Zhang Y, Cao F, Dong K, Ren J, et al. Erythrocyte membrane cloaked metal-organic framework nanoparticle as biomimetic nanoreactor for starvation-activated colon cancer therapy. *ACS Nano* 2018;**12**:10201−11.
28. Yang S, Tang Z, Hu C, Zhang D, Shen N, Yu H, et al. Selectively potentiating hypoxia levels by Combretastatin A4 nanomedicine: toward highly enhanced hypoxia-activated prodrug Tirapazamine therapy for metastatic tumors. *Adv Mater* 2019;**31**:e1805955.
29. Yang Z, Chi D, Wang Q, Guo X, Lv Q, Wang Y. Improved antitumor activity and tolerability of cabazitaxel derived remote-loading liposomes. *Int J Pharm* 2020;**589**:119814.
30. Zhao D, Tao W, Li S, Chen Y, Sun Y, He Z, et al. Apoptotic body-mediated intercellular delivery for enhanced drug penetration and whole tumor destruction. *Sci Adv* 2021;**7**:eabg0880.
31. Pitchaimani A, Nguyen TDT, Aryal S. Natural killer cell membrane infused biomimetic liposomes for targeted tumor therapy. *Biomaterials* 2018;**160**:124−37.
32. He Y, Li R, Li H, Zhang S, Dai W, Wu Q, et al. Erythroliposomes: integrated hybrid nanovesicles composed of erythrocyte membranes and artificial lipid membranes for pore-forming toxin clearance. *ACS Nano* 2019;**13**:4148−59.
33. Litvinov RI, Barsegov V, Schissler AJ, Fisher AR, Bennett JS, Weisel JW, et al. Dissociation of bimolecular αIIbβ3-fibrinogen complex under a constant tensile force. *Biophys J* 2011;**100**:165−73.
34. Sanchez-Gaytan BL, Fay F, Hak S, Alaarg A, Fayad ZA, Pérez-Medina C, et al. Real-time monitoring of nanoparticle formation by FRET imaging. *Angew Chem Int Ed Engl* 2017;**56**:2923−6.
35. Hanley WD, Napier SL, Burdick MM, Schnaar RL, Sackstein R, Konstantopoulos K. Variant isoforms of CD44 are P- and L-selectin ligands on colon carcinoma cells. *FASEB J* 2006;**20**:337−9.
36. Zhou Z, Zhang B, Wang S, Zai W, Yuan A, Hu Y, et al. Perfluorocarbon nanoparticles mediated platelet blocking disrupt vascular barriers to improve the efficacy of oxygen-sensitive antitumor drugs. *Small* 2018;**14**:e1801694.
37. Tao W, He Z. ROS-responsive drug delivery systems for biomedical applications. *Asian J Pharm Sci* 2018;**13**:101−12.
38. Wieczorek E, Mlynarczyk DT, Kucinska M, Dlugaszewska J, Piskorz J, Popenda L, et al. Photophysical properties and photocytotoxicity of free and liposome-entrapped diazepinoporphyrazines on LNCaP cells under normoxic and hypoxic conditions. *Eur J Med Chem* 2018;**150**:64−73.
39. Sadzuka Y, Tokutomi K, Iwasaki F, Sugiyama I, Hirano T, Konno H, et al. The phototoxicity of photofrin was enhanced by PEGylated liposome *in vitro*. *Cancer Lett* 2006;**241**:42−8.
40. Li L, Liu Y, Li H, Guo X, He X, Geng S, et al. Rational design of temperature-sensitive blood-vessel-embolic nanogels for improving hypoxic tumor microenvironment after transcatheter arterial embolization. *Theranostics* 2018;**8**:6291−306.
41. Rankin EB, Giaccia AJ. Hypoxic control of metastasis. *Science* 2016;**352**:175−80.